UNIVERSITY OF AMSTERDAM

UvA-DARE (Digital Academic Repository)

Imaging of the human subthalamic nucleus

Alkemade, A.; Forstmann, B.U.

DOI
[10.1016/B978-0-12-820107-7.00025-2](https://doi.org/10.1016/B978-0-12-820107-7.00025-2)

Publication date
2021

Document Version
Final published version

Published in
The Human Hypothalamus

License
Article 25fa Dutch Copyright Act

[Link to publication](#)

Chapter 25

Imaging of the human subthalamic nucleus

ANNEKE ALKEMADE AND BIRTE U. FORSTMANN*

Integrative Model-Based Cognitive Neuroscience Research Unit, University of Amsterdam, Amsterdam, The Netherlands

Abstract

The human subthalamic nucleus (STN) is a small lens shaped iron rich nucleus, which has gained substantial interest as a target for deep brain stimulation surgery for a variety of movement disorders. The internal anatomy of the human STN has not been fully elucidated, and an intensive debate, discussing the level of overlap between putative limbic, associative, and motor zones within the STN is still ongoing. In this chapter, we have summarized anatomical information obtained using different neuroimaging modalities focusing on the anatomy of the STN. Additionally, we have highlighted a number of major challenges faced when using magnetic resonance imaging (MRI) approaches for the visualization of small iron rich deep brain structures such as the STN. In vivo MRI and *postmortem* microscopy efforts provide valuable complementary information on the internal structure of the STN, although the results are not always fully aligned. Finally, we provide an outlook on future efforts that could contribute to the development of an integrative research approach that will help with the reconciliation of seemingly divergent results across research approaches.

INTRODUCTION

The human subthalamic nucleus (STN) is a biconvex-shaped structure located above the cerebral peduncle, which contains approximately 550,000 neurons (Parent et al., 1996). The STN is part of the basal ganglia network which, together with cortex, controls the execution of planned motivated behavior involving motor, cognitive, and limbic circuits (Haber, 2003). The seminal work by Bergman et al. (1990), showing that lesioning of the STN reversed experimental 1-methyl-4-phenyl-1,2,3,6-tetrahydropyridine (MPTP) parkinsonism in monkeys has formed the scientific basis for the development of current deep brain stimulation (DBS) procedures targeting the STN in a variety of neuromotor diseases. The development of DBS has sparked a strong scientific and clinical interest in the structure and function of the STN. Together with the increasing interest, imaging efforts to visualize the human STN in vivo have become increasingly successful due to the development of

ultra-high-resolution 7 Tesla (T) magnetic resonance imaging (MRI) systems, as well as the adaptation of MRI sequences to accommodate the tissue properties of the STN and its surrounding tissue. Unfortunately, despite the dramatic improvements that have been made in the visualization of the STN, in vivo neuroimaging approaches continue to pose challenges. To date, there is no consensus on which neuroimaging technique is best to visualize the STN for surgical planning (Brunenberg et al., 2011). As a result, methods vary greatly between centers, and some groups apply indirect visualization techniques using anatomical landmarks and/or atlases that incorporate anatomical and functional data. The alternative approach includes direct visualization and is reported using a variety of MRI contrasts (Brunenberg et al., 2011).

In general, neuroimaging approaches and the associated compromises are chosen to match the clinical or basic research question at hand. Based on the purpose

---

*Correspondence to: Birte U Forstmann, Ph.D., Integrative Model-based Cognitive Neuroscience (IMCN) research unit, University of Amsterdam, Nieuwe Achtergracht 129B | Room G3.06, PO Box 15926 | 1001 NK Amsterdam, The Netherlands. Tel: + 31-6-15324988, E-mail: buforstmann@gmail.com

for which the STN is imaged, a number of factors affecting the imaging procedure are weighed and together determine the imaging strategy. In this chapter, we will discuss different approaches for the neuroimaging of the STN for clinical and research purposes, as well as the underlying functional neuroanatomy of the nucleus including the challenges associated with fMRI studies of the STN. Finally, we will discuss to what extent in vivo neuroimaging data can be merged with the underlying functional neuroanatomy of the STN.

IN VIVO NEUROIMAGING OF THE STN

For in vivo neuroimaging of the human STN, MRI represents the method of choice (Forstmann et al., 2017b). MRI techniques are based on the imaging of the magnetic behavior of atomic nuclei with a net positive charge (Grover et al., 2015). Even though MRI techniques are based on the same principle, the obtained images vary as a result of differences in the used hardware, applied scan sequences, as well as data postprocessing and contrast calculations. Together, this has resulted in a plethora of different types of MRI images of the brain. STN MRI is notoriously challenging due to the physical location of the nucleus, which is tucked away deep in the crowded subcortex, at a large, nearly equal distance from the MR receiver coils. Additionally, the STN directly borders the substantia nigra, which, like the STN, contains high concentrations of iron (de Hollander et al., 2014). MRI acquisition strategies for imaging of the STN reported in literature wildly vary, and the applied methods are dependent on the availability of hardware, implemented scan sequences, as well as the purpose for which the STN is imaged. In this chapter, we do not intend to provide an overview of all in vivo STN neuroimaging efforts that are available in the literature. We will discuss a number of crucial factors in the MRI imaging protocol that can be optimized to achieve the best account possible of the internal structure of the human STN, as well as comparisons across groups.

Benefits of high MRI field strength

An increasing number of 7 T MRI scanners are available for brain imaging purposes (Forstmann et al., 2017a; Keuken et al., 2018; Ladd et al., 2018). Theoretically, higher field strengths allow for better signal-to-noise and contrast-to-noise ratios, and following that line of reasoning, higher field strengths can deliver better brain images (Kraff et al., 2015; Trattnig et al., 2018). Additionally, a more powerful gradient system, available in a subset of MRI systems, will further benefit the obtained image quality. The use of 7 T MRI is still largely confined to research protocols, whereas for clinical imaging purposes, 1.5 or 3 T is commonly applied. In DBS,

neurosurgeons are also guided by other information, such as brain atlases, and information that is obtained intraoperatively, including electrophysiological assessments, and the direct clinical effect induced by the insertion of the electrode (Lozano et al., 2019). These assessments together allow for a reliable positioning of the electrode for surgical purposes.

Although 7 T MRI systems with powerful gradients are best suited for direct imaging of the STN, visualization using a 7 T scanner with a less powerful gradient system, or a more commonly available clinically approved 3 T scanner can also be achieved in a reliable fashion (Fig. 25.1). For each MRI system, image quality can be optimized by investing in the development of tailored scan acquisition protocols (de Hollander et al., 2017). Additionally, the averaging of multiple scan repetitions will benefit the MRI contrast, although this will increase scan times. Surprisingly, clinically implemented scan sequences are usually not optimized for STN imaging (Alkemade et al., 2017). Finally, the optimal contrast may differ between field strengths, which further complicates the interpretation of literature reports, and further complicates the choice for MRI contrasts based on available studies (Keuken et al., 2016; Bot et al., 2019).

Isotropy

A logical MRI parameter to optimize for the visualization of the three-dimensional (D) STN is the voxel size. In general, smaller voxel volumes are preferred. However, not only voxel volume but also voxel shape should be considered (Mulder et al., 2019). Isotropic voxels are voxels with the same dimension in every direction. Nonisotropic voxels are voxels that provide a high in-plane resolution combined with a relatively larger slice thickness, resulting in rod-shaped voxels. The application of high in-plane resolution in combination with a larger slice thickness allows for a clear identification of smaller structures such as the STN in a single plane, and often a single slice. For studies focused on larger brain structures, size and shape of the individual voxels will have limited effects on the anatomical delineation and size estimates of a structure. The effects for smaller nuclei in the brain can, however, be detrimental. To quantify the effects of voxel size on STN imaging in a systematic fashion, we performed simulation studies in which we varied voxel size, shape, and imaging orientation on an ellipsoid representative in size for the STN (Mulder et al., 2019). We found that larger slice thickness, reflecting a stronger anisotropy resulted in a more substantial overestimation of the structure volume (Fig. 25.2). Importantly, volume estimates consistently deviated more than 50% from their predefined volume when slice thickness had a threefold anisotropy for a resolution of
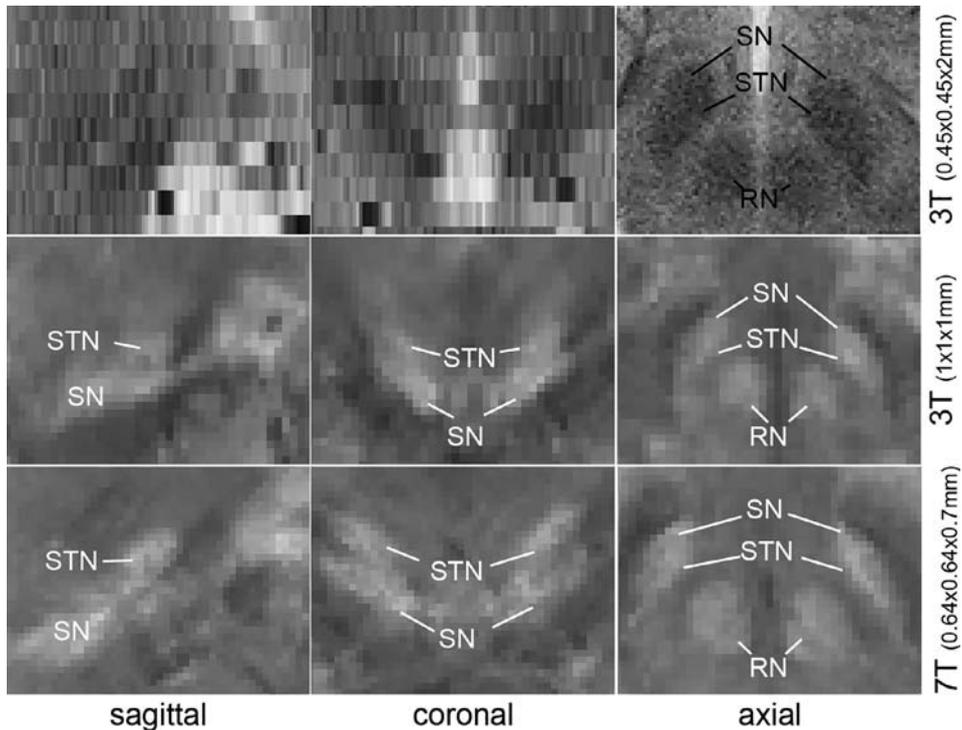
Fig. 25.1. Comparisons of MRI contrasts for the visualization of the healthy human subthalamic nucleus (STN). The upper panels show STN visibility using a 3 Telsa (T) T2-weighted image with anisotropic voxels, representative for clinical MRI imaging, which does not allow discerning of the STN in the sagittal and coronal view. The second row of panels shows the STN in QSM contrasts of the same subject, using an optimized 3 T scan. The bottom row shows QSM contrasts of the same subject in an optimized 7 T image. Note the improved STN-SN border visibility in the coronal 7 T contrast. The red nucleus (RN) and substantia nigra (SN) are indicated for anatomical orientation.

1.0×1.0 mm in-plane voxel size (Mulder et al., 2019). Given that the average voxel volume used for the visualization of subcortical structures on 7 T MRI reported in the scientific literature is 1.09mm^3 (Keuken et al., 2018), and voxels >1 mm isotropic are common, it is clear that further optimization of voxel size and shape represents a step forward.

(Quantitative) MRI characteristics of the STN

As compared to cortical brain areas, the STN and other nuclei of the basal ganglia have high iron concentrations (Schafer et al., 2012; Deistung et al., 2013; de Hollander et al., 2014; Birkl et al., 2016; Alkemade et al., 2017). The high iron content affects MRI parameters, causing a substantial shortening of the T1 and T2 relaxation times. This means that for optimal imaging of the STN, echo times of the scan sequence need to be substantially shorter than echo times commonly used to image the neocortex (Schafer et al., 2012; Forstmann et al., 2017b). Interestingly, the iron concentrations can also be used to improve imaging quality, and they can serve as input for quantitative MRI studies.

Quantitative MRI refers to the calculation and analyses of maps that project meaningful physical or chemical variables that can be expressed in physical units and compared between and within tissue regions among individuals (Pierpaoli, 2010). The read out of multiple echo's allows the detection of small susceptibility changes, as well as correction for multiexponential T2*-decay (Stüber et al., 2014). These parameters can be used for the calculation of iron concentrations in the STN, by means of quantitative susceptibility mapping (QSM) (Stüber et al., 2014). Detailed analyses of QSM contrasts of the STN have demonstrated an inhomogeneous distribution of iron within the nucleus, more specifically, an iron gradient, with highest iron concentrations in the ventromedial part of the nucleus (de Hollander et al., 2014). The demonstration of the iron gradient illustrates the potential value of MRI and more specifically QSM for studies targeting the internal structure of the STN in vivo. Quantitative comparisons of delineations made independently on QSM and T2* contrasts in volunteers with and without Parkinson's disease revealed that QSM contrasts give a higher interrater agreement as compared to T2* (Alkemade et al., 2017) (Fig. 25.3). This can be interpreted as an improved
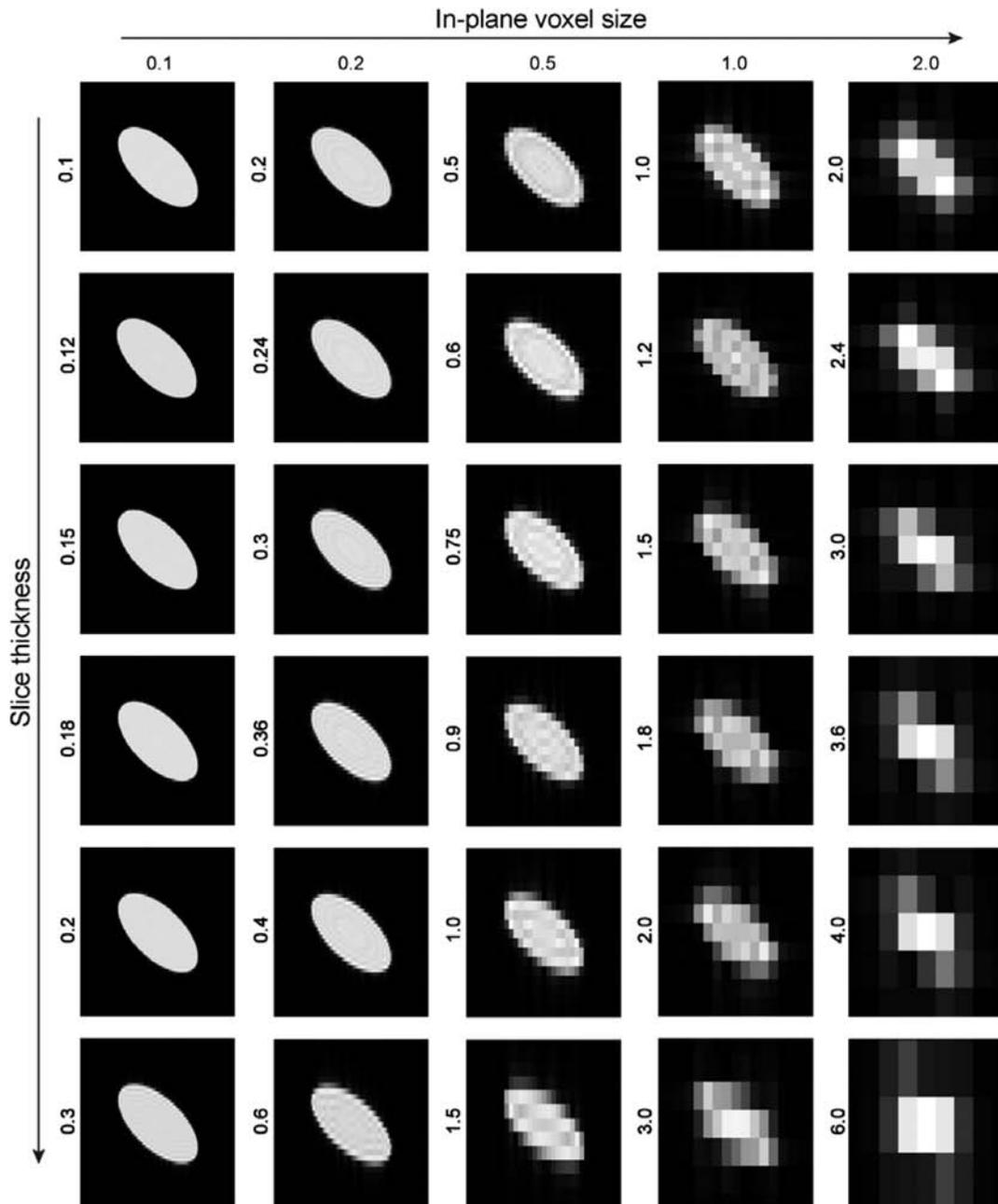
Fig. 25.2. Simulations of the effects of voxel shape and size on the visualization of the human STN, which is represented as an ellipsoid. Note the deformations resulting from the increase in slice thickness. Reproduced with permission from Mulder MJ et al. (2019). Size and shape matter: the impact of voxel geometry on the identification of small nuclei. PLoS One 14: e0215382. Bergsland N (Ed.). doi: 10.1371/journal.pone.0215382. Public Library of Science.

visibility of the STN (Alkemade et al., 2017). Interestingly, particularly volunteers with Parkinson's disease benefitted from the use of iron sensitive contrasts, stressing the potential benefit of sequence optimization and the implementation of iron sensitive contrasts for clinical purposes (Fig. 25.3) (Alkemade et al., 2017). It is important to note that QSM, which is calculated using the phase images, can vary with the use of different calculation protocols. The use of various methods of calculation

complicate direct comparisons between studies available from scientific literature.

Interindividual variation of STN volume and location

In vivo MRI measurements of the STN allow the study of a larger number of individuals as compared to *postmortem* analyses to obtain estimations of the variability in
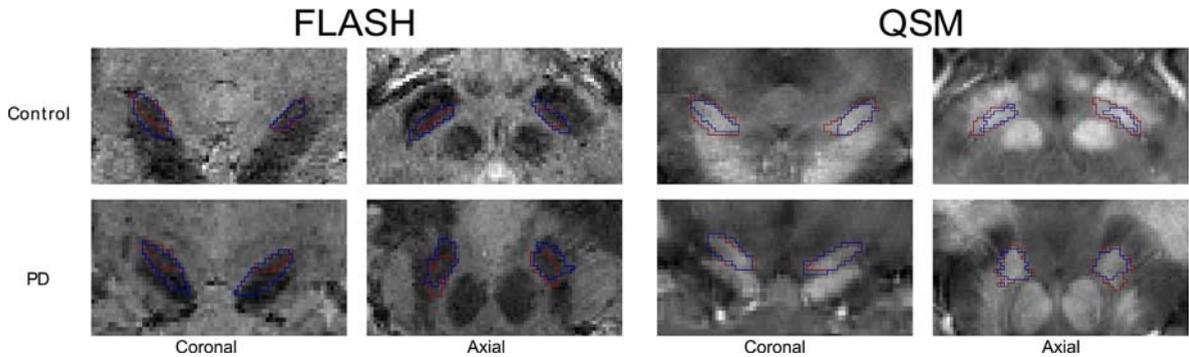
Fig. 25.3. STN visualization in T2*-weighted and QSM contrasts calculated from a single MRI scan. The *red* and *blue* outlines represent the independent delineations by two raters. Note the increased agreement in the QSM images, which was particularly higher in volunteers with Parkinson's disease (PD). Figure was reproduced from Alkemade A et al. (2017). Comparison of T2*-weighted and QSM contrasts in Parkinson's disease to visualize the STN with MRI. PLoS One 12: e0176130. Jiang Q (Ed.). doi: 10.1371/journal.pone.0176130. Public Library of Science, with permission.

Table 25.1

Volume estimations of the human subthalamic nucleus

STN volume (mm^3)	Applied method	References
64	Microscopy	Fussenich (1967)
120	Microscopy	Hardman et al. (2002)
175	Microscopy	Levesque and Parent (2005)
141	Microscopy	Lange et al. (1976)
106	MRI 9.4 T	Massey et al. (2012)
174	Microscopy	Nowinski et al. (2005)
100.5	MRI 7.0 T	Plantinga et al. (2016)
157	Microscopy	von Bonin and Shariff (1951)
109	MRI 7.0 T	Weiss et al. (2015)
180	Microscopy	Yelnik and Percheron (1979)
99	MRI 3.0 T	Zwirner et al. (2017)
131	Microscopy	Zwirner et al. (2017)
Average: 129.7 (SD 36.5)		

Adapted from Mulder MJ et al. (2019). Size and shape matter: the impact of voxel geometry on the identification of small nuclei. PLoS One 14: e0215382. Bergsland N (Ed.). doi: 10.1371/journal.pone.0215382. Public Library of Science.

STN volume, as well as location. As described previously, MRI results are strongly dependent on the MRI acquisition protocol, as well as on the contrast calculations and data analyses.

Size estimates of the *postmortem* STN are available from literature and are summarized in Table 25.1. On average the size of the STN is 129.7 mm^3. Numbers obtained from in vivo MRI are often based on conjunct volumes, which only include voxels included in STN delineations by two independent researchers (Keuken et al., 2013; Keuken and Forstmann, 2015; Alkemade et al., 2017). As a consequence of the chosen method of analysis, these numbers represent a conservative estimation of STN size. We initially reported an average

conjunct STN volume in healthy volunteers of 69.2 mm^3 when the STN was delineated on T2*-weighted images. Using the QSM contrast, we found that the observed STN volume became substantially larger (82.34 mm^3) (Alkemade et al., 2017). Similar findings were present in volunteers with PD. The observed increase in STN volume could be explained by improved visibility of the STN in QSM images, which was evidenced by higher interrater agreement scores (Dice and Dice, 1945; Alkemade et al., 2017). Interestingly, size estimates were not affected by age, but the location of the STN shifts in lateral directions with increasing age. This effect could not be explained by widening of the ventricular cavities as a result of aging, and warrants replication as well as further investigation (Keuken et al., 2013).

Diffusion-weighted imaging

Resolving the connectivity profile of the STN could represent another approach to understand the internal structure of the human STN. Lambert et al. (2012) have made the first step in using probabilistic tractography to estimate the spatial distribution of white matter pathways. This study confirmed the presence of white matter connections to other limbic, associative, and motor brain regions. A large proportion of the STN voxels contained mixed connection profiles corresponding to limbic, associative, and motor functions of the STN. The question rises whether this could be attributed to partial volume effects, or whether connection profiles are highly intermixed within the STN (Alkemade and Forstmann, 2014). Further development of DWI techniques is needed to resolve this question.

Functional (f)MRI

The STN is implicated in action selection, cognitive control, and response inhibition (Alexander and Crutcher, 1990; Parent and Hazrati, 1995; Redgrave et al., 1999;

Middleton and Strick, 2000; Frank, 2006; Aron, 2011). Measurements of blood oxygenation level-dependent MRI allow assessment of brain activity (Ogawa et al., 1990), and to target questions on STN function, development of fMRI approaches are a logical step. These have proven to be technically challenging, since the size of 3 T fMRI voxels is commonly in the range of 3 mm isotropic (de Hollander et al., 2017). Given the size of the STN, this results in fewer than 5 voxels per STN, which are likely to suffer from partial voluming effects, and therefore may also incorporate signal from adjoining structures including the substantia nigra, and the lateral hypothalamus (de Hollander et al., 2015, 2017). These challenges are further aggravated in fMRI studies using standardized analysis techniques for which the individual brain scans are registered to a standard space, which does not accommodate the interindividual variation in the anatomy of the basal ganglia (de Hollander et al., 2017).

Despite these challenges, several groups have made efforts to target the STN region using functional MRI. Pathways between the STN and the inferior frontal cortex, as well as the presupplementary motor area were investigated (Aron et al., 2007), followed by investigations on the connectivity between the STN and the presupplementary motor area, primary motor cortex, anterior cingulate cortex inferior frontal gyrus, and the striatum (Forstmann et al., 2010). STN regions of interest were tested for their connections to motor, associative, and limbic areas in the brain (Brunenberg et al., 2011). A recent careful comparison of 3 and 7 T fMRI protocols has revealed increased STN activation in failed stop trials as compared with successful stop and go trials (de Hollander et al., 2017). These studies were performed using a robust stop-signal paradigm (Logan et al., 1984; Aron and Poldrack, 2006). Interestingly, not only the STN, but also the substantia nigra, the red nucleus, and the globus pallidus (internal and external segment) showed this activation pattern. The coactivation of these individual basal ganglia nuclei together with the partial voluming effects in fMRI call for caution in the interpretation of available fMRI studies on the STN, and further technical developments are needed to address these challenges.

THE MICROSCOPIC ANATOMY OF THE STN

Despite the strong interest in the STN, the number of publications that show a detailed investigation of protein expression in the human STN is limited (Alkemade et al., 2015). Studies addressing the internal anatomy of the STN at a cyto- and immunocytochemical level only represent a minor fraction of the available body of literature on the human STN and predominantly consists of older

studies. An additional limited body of literature is available on the internal structure of the STN in nonhuman primates (Alkemade et al., 2015). Like any other brain structure studied in the human *postmortem* brain, studies of the human STN are limited by the low number of available tissue specimens. Putative confounding factors in studies on human *postmortem* brain specimens include sex, age, brain weight, agonal state, seasonal and circadian variation, lateralization, as well as tissue treatment, including *postmortem* delay, fixation duration, and storage time. Available literature almost exclusively consists of qualitative assessments of distribution patterns of individual proteins or mRNA transcripts. Differences in antibody characteristics, as well as staining protocols including staining amplification, preclude quantitative comparisons between immunoreactivity distribution patterns for different protein markers, even within the same specimens. Comparisons across studies reported literature are therefore usually limited to qualitative assessments.

Immunoreactivity in the human STN

Calcium-binding proteins have been used to identify individual populations of interneurons in the basal ganglia including the STN (Parent et al., 1996). Calretinin (CALR) positive neurons were reported to be concentrated in the ventromedial part of the STN, whereas parvalbumin (PARV) positive neurons showed a more dense distribution in the dorsolateral part of the STN (Parent et al., 1996; Augood et al., 1999; Morel et al., 2002). Additional studies from our group investigating 10 STNs from nondemented controls showed slightly different results for PARV (Fig. 25.4). We replicated the labeling of PARV neurons in the ventromedial region of the STN and found that their staining was more abundant in the dorsal parts of the STN. However, highest intensities were observed in the medial parts of the dorsal extent of the STN, not the lateral areas (Alkemade et al., 2019). It remains unknown what causes this difference. In these studies we also found that CALR showed strongest neuronal labeling in the ventromedial tip of the human STN, thereby replicating earlier findings (Parent and Hazrati, 1995; Alkemade et al., 2019). Together these findings suggest regional differences in calcium signaling within the human STN. The dorsal part of the STN tip appears to be predominantly dependent on PARV, and to a lesser extent on CALR, which showed highest expression levels in the ventromedial part of the STN.

Two studies are available on the expression of neurofilament (SMI32) staining in the human STN (Morel et al., 2002; Alkemade et al., 2019). Morel et al. (2002) described the distribution of SMI32 as similar to that of
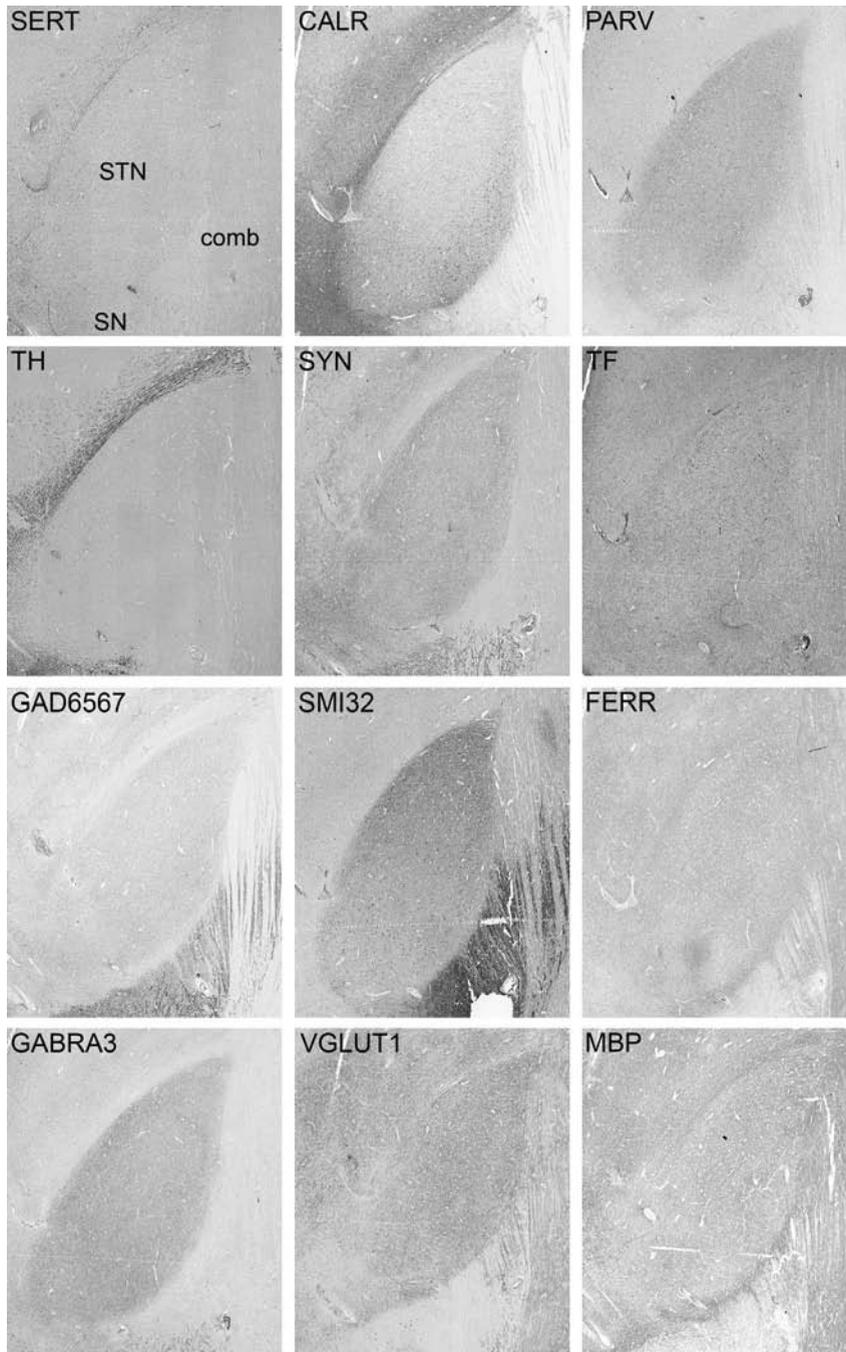
Fig. 25.4. Example of immunoreactivity in a single specimen for serotonin transporter (SERT), calretinin (CALR), parvalbumin (PARV), tyrosine hydroxylase (TH), synaptophysin (SYN), transferrin (TF), glutamic acid decarboxylase (GAD65/67), neurofilament H (SMI32), ferritin (FERR), GABA receptor subunit A3 (GABRA3), vesicular glutamate transporter 1 (VGLUT1), and myelin basic protein (MBP). *Comb*, comb system; *SN*, substantia nigra; *STN*, subthalamic nucleus. Image was reproduced from Alkemade A, de Hollander G, Miletic S, Keuken Max C et al. (2019). The functional microscopic neuroanatomy of the human subthalamic nucleus. Brain Struct Funct 224: 3213–3227. doi: 10.1007/s00429-019-01960-3. Springer Berlin Heidelberg, with permission.

CALR with relatively weak staining in the neuropil and intense staining resembling Golgi stains in neurons distributed along the border of the STN. Most intense staining was observed in the ventromedial part of the STN.

These observations differed from our later quantitative analyses, which revealed a relatively low expression of SMI32 in the ventromedial parts of the STN (Alkemade et al., 2019). Staining clear labeling of the neuronal cell

bodies with a gradual decrease in intensity in the ventromedial direction, where weaker neuronal labeling was observed. The effect was most pronounced in the anterior STN. In the caudal regions of the STN, staining was more uniform. Weak fiber staining was also observed. Long thin fibers were occasionally stained in the dorsolateral part of the STN. Although less pronounced, a similar gradual decrease in fiber staining was observed in the ventromedial direction. It is also possible that differences in SMI-32 expression are associated with different axonal lengths and projection sites, or that the discrepancy between Alkemade et al. (2019) and the study by Morel et al. (2002) is the result of differences in the sampling procedure. The quantitative results we presented in our studies were obtained from a systematic 300 μm sampling interval, whereas the studies by Morel et al. (2002) followed a more descriptive approach.

For synaptophysin punctate, staining was scattered throughout the nucleus. Staining density of the presynaptic terminals or boutons appeared higher in the ventromedial and dorsolateral parts of the nucleus indicating intense communication with cells in this area. Interestingly, punctate staining extended beyond the dorsolateral tip of the nucleus in the shape of a cap. At the caudal level, the staining was more homogeneous. Furthermore, neuronal somata surrounded by puncta were detected, scattered throughout the nucleus (Alkemade et al., 2019).

There are several candidate neurotransmitters for the dense input in the ventromedial part of the STN. Markers for proteins involved in GABA-ergic, glutamatergic, serotonergic, and dopaminergic signaling are all expressed in the STN.

The strong glutamatergic output of the STN, which projects to the main basal ganglia output structures, is reflected by the presence of glutamate, and the expression of metabotropic glutamate receptors in the monkey STN (Smith and Parent, 1988; Parent and Hazrati, 1995; Kuwajima et al., 2004) as well as punctate vesicular glutamate transporter 1 staining in the human STN (Alkemade et al., 2019). A minority of STN cells express glutamate decarboxylase, which is indicative of local glutamate to GABA conversion (Levesque and Parent, 2005; Alkemade et al., 2019).

The expression of the GABA transporter (GAT)1, which removes GABA from the synaptic cleft, shows a more general distribution in the human STN (Smith and Parent, 1988; Augood et al., 1999; Hirunsatit et al., 2009). GABA-A and B receptors have been identified both in human and monkey STN, through the use of immunocytochemistry and in situ hybridization, respectively (Kultas-Ilinsky et al., 1998; Charara et al., 2000; Alkemade et al., 2019). In humans GABA receptor type A, alpha 3 subunit showed a higher staining intensity in the ventromedial part of the nucleus (Alkemade et al., 2019). Additionally, a minority of the neurons displayed Glutamate decarboxylase (GAD65/67) immunoreactivity, again with a higher staining intensity in the ventromedial part of the nucleus, indicating that GABA-ergic signaling was not homogeneously distributed throughout the STN (Alkemade et al., 2019).

The expression of type 1 and 2 dopamine receptors (D1R and D2R) has been described by two independent studies using radioactive in situ hybridization studies (Augood et al., 2000; Hurd et al., 2001). Both studies were able to detect D1R expression, but only Hurd et al. (2001), and not Augood et al. (2000) reported the detection of D2R mRNA. It is feasible that D2R mRNA expression levels did not reach the detection threshold in the studies by Augood et al. (2000) and these studies warrant replication using more sensitive techniques. Expression of tyrosine hydroxylase (TH), the rate-limiting enzyme in catecholamine synthesis, and thereby crucial for dopamine production was described originally by Hedreen (1999). In these studies, the authors showed that the majority of immunoreactive axons passed over and through the STN, with occasional branching in the STN, which was interpreted as indicative of STN innervation (Hedreen, 1999). Later studies by our group confirmed TH innervation, demonstrating both thick long and thin punctate fibers, with a clear gradient in the medial-lateral direction with highest fiber density in the ventromedial part of the STN (Alkemade et al., 2019).

Serotonergic innervation of the monkey STN was reported by Parent et al. (2011), who described a clear topological organization of serotonin transporter (SERT) immunoreactivity within the STN, with a stronger innervation of its anterior half. The human STN shows comparable SERT distribution, with clear SERT fiber staining showing a graded density decreasing in the lateral direction, with highest densities observed in the ventromedial tip. Fiber densities in the dorsolateral two-thirds of the nucleus were low. This effect was most pronounced in anterior and central parts of the STN, and a general decrease in staining intensity was observed in the caudal extent of the nucleus (Alkemade et al., 2019). These findings are in line with serotonin (5HT) distribution patterns observed in monkeys (Mori et al., 1985). 5HT density was highest in the more medial and ventral parts of the STN, with rostral scattered fiber tracts, and fiber segments oriented toward the lateral margin of the STN (Mori et al., 1985).

Older studies described the expression of endogenous opioid receptors using RNA blotting (Raynor et al., 1995), revealing transcripts in the STN, and preproenkephalin B was reported in the STN of monkeys, including an increased expression during levodopa treatment in

experimental Parkinson's disease (Aubert et al., 2007). As discussed previously, only a limited number of studies investigating the internal structure of the STN have been published. In addition to valuable descriptions of the distribution of immunoreactivity targeting proteins that are expressed in the STN, it is possible that more studies on the STN have been conducted, yielding negative results. These studies may not have made their way into the scientific literature due to a publication bias (Ioannidis, 2005). We therefore consider it also of importance to report on proteins targeted in immunocytochemical studies, and which did not reveal clear staining patterns in the STN (Alkemade et al., 2019). NPY and CRH did not show expression in the STN, and Orexin A only showed sporadic immunopositive fibers as did vasoactive intestinal polypeptide and somatostatin. Aromatase labeled a few STN neurons in a single subject, and ChAT staining revealed sporadic immunoreactive boutons (Alkemade et al., 2019).

Comparing microscopy studies to MRI

Additionally, we would like to mention the histological and immunocytochemical staining of molecules that are of potential interest in the translation across modalities used for investigations of the STN. From MRI studies it is clear that iron is of great interest to study the internal structure of the STN. Perl staining was used for validation of MRI observations confirming that hyperintense areas on QSM and hypointense areas on T2*-weighted images corresponded iron rich brain structures (Dormont et al., 2004; Sun et al., 2015). In the STN immunoreactivity for transferrin, which controls the level of free iron available in the blood, was present in numerous blood vessels and oligodendrocytes. The oligodendrocytes displayed a rounded shape and were arranged in rows between fibers in the white matter regions. Signal was present in the rim of the cytoplasm. Neuronal staining was also observed, although less abundant as compared to oligodendrocytes. Neuronal labeling was cytoplasmic, and fiber staining was occasionally observed. Transferrin staining showed substantial background staining, which varied in intensity between subjects. This fits with transferrin labeling in the extracellular matrix. Transferrin also showed a lower staining intensity in the ventromedial part of the STN. Transferrin plays an important role in the delivery of iron to brain cells and is expressed in neurons as well as oligodendrocytes (Alkemade et al., 2019). Numerous ferritin positive oligodendrocytes were detected across the STN. Ferritin plays an important role in iron storage. The distribution of ferritin positive oligodendrocytes was quite uniform across the STN, as well as across subjects.

The question rises whether protein distribution patterns can be related to regional functional differences and distinct neuronal populations within the STN. In nonhuman primates, neurons located in the dorsolateral part of the STN are connected to the globus pallidus externa, whereas neurons connected to the globus pallidus interna, substantia nigra pars reticulate, and caudate nucleus are largely confined to the ventromedial parts of the STN (Nauta and Cole, 1978; Smith et al., 1990). In addition, neurons projecting to the ventral globus pallidus are located in the medial STN (Nauta and Cole, 1978; Smith et al., 1990). The ventromedial part of the human STN contains smaller neurons and shows a higher cell density as compared to more lateral regions (Fussenich, 1967). However, despite consistent distribution patterns across specimens, we observed considerable overlap in the staining patterns of markers, as well as considerable differences. Some markers extended beyond the borders of the STN, which appears to be at odds with older reports that the STN is a closed nucleus (Rafols and Fox, 1976).

It is difficult to speculate on the importance of the observed topographical variations in the mechanism underlying deep brain stimulation and their relation to functional subdivisions. According to the literature (Greenhouse et al., 2013), STN electrodes inserted to treat a number of motor and other disorders are aimed at the dorsolateral part of the STN. None of the tested markers was confined to the dorsolateral STN. Overlapping protein distribution patterns are in line with those of Haynes and Haber (2013), who showed significant overlap in projection patterns within the primate STN and the description of topographically arranged transition zones within the STN (Lambert et al., 2015).

COMPARING AND INTEGRATING IN VIVO MRI AND *POSTMORTEM* STUDIES

High-quality neuroanatomical research in humans is contingent on a constructive dialogue between those engaged in *postmortem* research defining underlying architectural properties and those attempting to model and capture these features using in vivo MRI (Lambert et al., 2015). To facilitate the dialogue between researchers performing *postmortem* studies and those involved in in vivo imaging of the STN, it is crucial to understand to what extent the applied techniques are comparable and results can be translated across modalities (Forstmann et al., 2017b).

Size measurements reported based on *postmortem* investigations using either MRI or microscopy approaches provide an estimation of the average STN size of 129.7 mm^3, which is substantially larger than that

observed using in vivo MRI techniques. In vivo MRI thus appears to provide an underestimation of the size of the STN. *Postmortem* estimations are based on a very low number of observations, and it is unclear whether this could have biased the results. Additionally, the majority of histological approaches do not provide a 3D account of the structure, which hampers volume estimations. At the same time, estimations from MRI images are dependent on the used MRI parameters and the calculated contrast. Given the inherent limitations associated with the individual research approaches, the separate research fields should be considered of complimentary value, and results from these individual fields would be expected to converge. Together the findings should contribute to an improved understanding of the structure and function of small human brain nuclei, including the STN. Further integration of the research approaches is expected to contribute to the resolving of potential discrepancies, and integration can aid in the cross validation of the individual imaging techniques. Furthermore the integration of research fields can provide a crucial contribution to resolve ongoing discussions on the structure and function of the human STN, which can be attributed, at least to some extent to the difficulties associated with the translation of results across research fields (Lambert et al., 2012; Alkemade and Forstmann, 2014). Such comparisons across modalities are gaining interest within the scientific community and often used for qualitative comparison in smaller tissue blocks, in some cases in combination with histological approaches (e.g., Bürgel et al., 1999; Castellanos et al., 2008; Makris et al., 2013; Adler et al., 2014; Annese et al., 2014; Augustinack et al., 2014; Plantinga et al., 2016).

Practical limitations of *postmortem* MRI investigations of the human brain include the impracticalities associated with the scanning of unfixed human brain tissue. Such experiments are dependent on the availability of fresh donor material and therefore difficult to plan. Scan duration is limited as a result of the tissue degradation after the demise of the donor. Therefore, often formalin fixed tissues are used for detailed MRI investigations, solving the problem of tissue degradation, but at the same time introducing other challenges. Formalin fixation affects the shape and MR characteristics of the tissue (Chu et al., 2005; Schmierer et al., 2008; van Duijn et al., 2011; Stüber et al., 2014). Additionally, often *postmortem* studies involve small tissue samples, which are then imaged using ultra-high-resolution MRI. Through adjustment of the MR characteristics, it is possible to visualize the STN in such tissue specimens with excellent detail (Massey et al., 2012). Remaining challenges include coregistration between specimens, and with MRI standard space, given the limited number of landmarks present in smaller samples for registration purposes. We have created a multistage approach, which allowed to coregister detailed anatomical scans of the STN to MNI space (Weiss et al., 2015), although registration of whole brain specimens would be preferred in view of the larger amount of shared information available for registration.

A logical, but challenging next step is to reconstruct whole human brains in 3D, for which impressive proof of concept was provided by Amunts et al. (2013) through the creation of BigBrain. BigBrain is a high-resolution 3D reconstruction of a whole human brain of a 64-year-old male, which was sliced in 20 μm sections, which were histologically processed and digitally coregistered (Amunts et al., 2013). The creation of BigBrain is exciting, showing that a whole human brain processed for microscopy purposes can be reconstructed. Unfortunately, the MRI data collected for BigBrain was limited in quality and therefore does not allow reliable identification of the STN on the MRI images. Exciting expected future developments that can be anticipated include the combination of state-of-the-art *postmortem* multimodal MRI imaging using ultra-high-field scanners, with subsequent coregistration of the data with 3D reconstructions of histological data using comparable techniques as used for the creation of BigBrain (Amunts et al., 2013). Such approaches will be invaluable for the cross validation of imaging techniques and for future studies that will contribute to the reconciliation of differences across research fields investigating the internal structure and function of the human STN.

CONCLUSION

The continuously growing interest in the structure and function of the STN, together with exciting technical advances in the field of MRI, have substantially increased our understanding of the structure and function of STN. The use of submillimeter isotropic voxels and iron sensitive contrasts are key to obtain reliable images in vivo, although functional MRI data should still be interpreted with caution in view of partial voluming effects, as well as interindividual variation. Ideally, *postmortem* studies would provide complementary and converging information providing the spatial resolution required to resolve the internal structure of the STN. However, discrepancies between findings from these research fields continue to exist. To understand the discrepancies between research fields and to potentially mitigate the shortcomings of the individual techniques, the integration of MRI and histological and immunocytochemical approaches is of great importance.

REFERENCES

Adler DH et al. (2014). Histology-derived volumetric annotation of the human hippocampal subfields in postmortem MRI. NeuroImage. Academic Press. 84: 505–523. https://doi.org/10.1016/J.NEUROIMAGE.2013.08.067.

Alexander GE, Crutcher MD (1990). Functional architecture of basal ganglia circuits: neural substrates of parallel processing. Trends Neurosci 13: 266–271. Available at http://www.ncbi.nlm.nih.gov/pubmed/1695401.

Alkemade A, Forstmann BU (2014). Do we need to revise the tripartite subdivision hypothesis of the human subthalamic nucleus (STN)? NeuroImage 95: 326–329, Elsevier Inc. https://doi.org/10.1016/j.neuroimage.2014.03.010.

Alkemade A, Schnitzler A, Forstmann BU (2015). Topographic organization of the human and non-human primate subthalamic nucleus. Brain Struct Funct 220: 3075–3086, Springer Berlin Heidelberg. https://doi.org/10.1007/s00429-015-1047-2.

Alkemade A et al. (2017). Comparison of T2*-weighted and QSM contrasts in Parkinson's disease to visualize the STN with MRI. PLoS One. Edited by Q. Jiang. Public library of science. 12: e0176130. https://doi.org/10.1371/journal.pone.0176130.

Alkemade A, de Hollander G, Miletic S et al. (2019). The functional microscopic neuroanatomy of the human subthalamic nucleus. Brain Struct Funct 224: 3213–3227. https://doi.org/10.1007/s00429-019-01960-3.

Amunts K et al. (2013). BigBrain: an ultrahigh-resolution 3D human brain model. Science 2013/06/22, 340: 1472–1475. https://doi.org/10.1126/science.1235381.

Annese J et al. (2014). Postmortem examination of patient H.M.'s brain based on histological sectioning and digital 3D reconstruction. Nat Commun 5: 3122, Nature Publishing Group. https://doi.org/10.1038/ncomms4122.

Aron AR (2011). From reactive to proactive and selective control: developing a richer model for stopping inappropriate responses. Biol Psychiatry 69: e55–e68. https://doi.org/10.1016/j.biopsych.2010.07.024.

Aron AR, Poldrack RA (2006). Cortical and subcortical contributions to stop signal response inhibition: role of the subthalamic nucleus. J Neurosci 26: 2424–2433. https://doi.org/10.1523/JNEUROSCI.4682-05.2006.

Aron AR et al. (2007). Triangulating a cognitive control network using diffusion-weighted magnetic resonance imaging (MRI) and functional MRI. J Neurosci 27: 3743–3752. https://doi.org/10.1523/JNEUROSCI.0519-07.2007.

Aubert I et al. (2007). Enhanced preproenkephalin-B-derived opioid transmission in striatum and subthalamic nucleus converges upon globus pallidus internalis in L-3,4-dihydroxyphenylalanine-induced dyskinesia. Biol Psychiatry 61: 836–844. https://doi.org/10.1016/j.biopsych.2006.06.038.

Augood SJ et al. (1999). Localization of calcium-binding proteins and GABA transporter (GAT-1) messenger RNA in the human subthalamic nucleus. Neuroscience 88: 521–534. Available at http://www.ncbi.nlm.nih.gov/pubmed/10197772.

Augood SJ et al. (2000). Localization of dopaminergic markers in the human subthalamic nucleus. J Comp Neurol 421: 247–255. Available at http://www.ncbi.nlm.nih.gov/pubmed/10813785.

Augustinack JC et al. (2014). MRI parcellation of ex vivo medial temporal lobe. NeuroImage Academic Press. 93: 252–259. https://doi.org/10.1016/J.NEUROIMAGE.2013.05.053.

Bergman H, Wichmann T, DeLong MR (1990). Reversal of experimental parkinsonism by lesions of the subthalamic nucleus. Science 249: 1436–1438, American Association for the Advancement of Science. https://doi.org/10.1126/science.2402638.

Birkl C et al. (2016). Effects of formalin fixation and temperature on MR relaxation times in the human brain. NMR Biomed 29: 458–465. https://doi.org/10.1002/nbm.3477.

Bot M, Verhagen O, Caan M et al. (2019). Defining the dorsal STN border using 7.0-T MRI: a comparison to microelectrode recordings and lower field strength MRI. Stereotact Funct Neurosurg 97: 153–159. https://doi.org/10.1159/000500109.

Brunenberg EJL et al. (2011). Magnetic resonance imaging techniques for visualization of the subthalamic nucleus. J Neurosurg 115: 971–984. https://doi.org/10.3171/2011.6.JNS101571.

Bürgel U et al. (1999). Mapping of histologically identified long fiber tracts in human cerebral hemispheres to the MRI volume of a reference brain: position and spatial variability of the optic radiation. NeuroImage 10: 489–499, Academic Press. https://doi.org/10.1006/NIMG.1999.0497.

Castellanos FX et al. (2008). Cingulate-precuneus interactions: a new locus of dysfunction in adult attention-deficit/hyperactivity disorder. Biol Psychiatry 63: 332–337. https://doi.org/10.1016/j.biopsych.2007.06.025.

Charara A et al. (2000). Pre- and postsynaptic localization of GABA(B) receptors in the basal ganglia in monkeys. Neuroscience 95: 127–140. Available at http://www.ncbi.nlm.nih.gov/pubmed/10619469.

Chu W-S et al. (2005). Ultrasound-accelerated formalin fixation of tissue improves morphology, antigen and mRNA preservation. Mod Pathol 18: 850–863, Nature Publishing Group. https://doi.org/10.1038/modpathol.3800354.

de Hollander G et al. (2014). A gradual increase of iron toward the medial-inferior tip of the subthalamic nucleus. Hum Brain Mapp 35: 4440–4449. https://doi.org/10.1002/hbm.22485.

de Hollander G, Keuken MC, Forstmann BU (2015). The subcortical cocktail problem; mixed signals from the subthalamic nucleus and substantia nigra. PLoS One 10: e0120572. https://doi.org/10.1371/journal.pone.0120572.

de Hollander G, Keuken MC, van der Zwaag W et al. (2017). Comparing functional MRI protocols for small, iron-rich basal ganglia nuclei such as the subthalamic nucleus at 7 T and 3 T. Hum Brain Mapp 38: 3226–3248. https://doi.org/10.1002/hbm.23586.

Deistung A et al. (2013). Toward in vivo histology: a comparison of quantitative susceptibility mapping (QSM) with magnitude-, phase-, and R2*-imaging at ultra-high magnetic

field strength. Neuroimage 2012/10/06, 65: 299–314. https://doi.org/10.1016/j.neuroimage.2012.09.055.

Dice LR, Dice (1945). Measurements of amount of ecologic association between species. Ecology 26: 297–302, Ecological Society of America. https://doi.org/10.2307/1932409.

Dormont D et al. (2004). Is the subthalamic nucleus hypointense on T2-weighted images? A correlation study using MR imaging and stereotactic atlas data. AJNR Am J Neuroradiol 25: 1516–1523. 2004/10/27. Available at http://www.ncbi.nlm.nih.gov/pubmed/15502130.

Forstmann BU et al. (2010). Cortico-striatal connections predict control over speed and accuracy in perceptual decision making. Proc Natl Acad Sci U S A 107: 15916–15920. https://doi.org/10.1073/pnas.1004932107.

Forstmann BU, Isaacs BR, Temel Y (2017a). Ultra high field MRI-guided deep brain stimulation. Trends Biotechnol 35: 904–907, Elsevier Ltd. https://doi.org/10.1016/j.tibtech.2017.06.010.

Forstmann BU et al. (2017b). Towards a mechanistic understanding of the human subcortex. Nat Rev Neurosci 18: 57–65, Nature Publishing Group. https://doi.org/10.1038/nrn.2016.163.

Frank MJ (2006). Hold your horses: a dynamic computational role for the subthalamic nucleus in decision making. Neural Netw 19: 1120–1136. https://doi.org/10.1016/j.neunet.2006.03.006.

Fussenich M (1967). Vergleichend anatomische studien uber den nucleus subthalamicus (corpus Luys) bei primaten, Ph.D. thesis, University of Freiburg.

Greenhouse I et al. (2013). Stimulation of contacts in ventral but not dorsal subthalamic nucleus normalizes response switching in Parkinson's disease. Neuropsychologia 51: 1302–1309. https://doi.org/10.1016/j.neuropsychologia.2013.03.008.

Grover VPB et al. (2015). Magnetic resonance imaging: principles and techniques: lessons for clinicians. J Clin Exp Hepatol 5: 246–255, Elsevier. https://doi.org/10.1016/j.jceh.2015.08.001.

Haber SN (2003). The primate basal ganglia: parallel and integrative networks. J Chem Neuroanat 26: 317–330. Available at: http://www.ncbi.nlm.nih.gov/pubmed/14729134.

Hardman CD et al. (2002). Comparison of the basal ganglia in rats, marmosets, macaques, baboons, and humans: volume and neuronal number for the output, internal relay, and striatal modulating nuclei. J Comp Neurol Wiley Subscription Services, Inc., A Wiley Company. 445: 238–255. https://doi.org/10.1002/cne.10165.

Haynes WIA, Haber SN (2013). The organization of prefrontal-subthalamic inputs in primates provides an anatomical substrate for both functional specificity and integration: implications for basal ganglia models and deep brain stimulation. J Neurosci Society for Neuroscience. 33: 4804–4814. https://doi.org/10.1523/JNEUROSCI.4674-12.2013.

Hedreen JC (1999). Tyrosine hydroxylase-immunoreactive elements in the human globus pallidus and subthalamic nucleus. J Comp Neurol 409: 400–410. Available at http://www.ncbi.nlm.nih.gov/pubmed/10379826.

Hirunsatit R et al. (2009). Twenty-one-base-pair insertion polymorphism creates an enhancer element and potentiates SLC6A1 GABA transporter promoter activity. Pharmacogenet Genomics 19: 53–65. https://doi.org/10.1097/FPC.0b013e328318b21a.

Hurd YL, Suzuki M, Sedvall GC (2001). D1 and D2 dopamine receptor mRNA expression in whole hemisphere sections of the human brain. J Chem Neuroanat 22: 127–137. Available at http://www.ncbi.nlm.nih.gov/pubmed/11470560.

Ioannidis JPA (2005). Why most published research findings are false. PLoS Med 2: e124, Public Library of Science. https://doi.org/10.1371/journal.pmed.0020124.

Keuken MC, Forstmann BU (2015). A probabilistic atlas of the basal ganglia using 7 T MRI. Data Brief 4: 577–582. https://doi.org/10.1016/j.dib.2015.07.028.

Keuken MC et al. (2013). Ultra-high 7T MRI of structural age-related changes of the subthalamic nucleus. J Neurosci 33: 4896–4900. https://doi.org/10.1523/JNEUROSCI.3241-12.2013.

Keuken MC, Schäfer A, Forstmann BU (2016). Can we rely on susceptibility-weighted imaging (SWI) for subthalamic nucleus identification in deep brain stimulation surgery? Neurosurgery 79: e945–e946. https://doi.org/10.1227/NEU.0000000000001395.

Keuken MC, Isaacs BR, Trampel R et al. (2018). Visualizing the human subcortex using ultra-high field magnetic resonance imaging. Brain Topogr 31: 513–545. https://doi.org/10.1007/s10548-018-0638-7.

Kraff O et al. (2015). MRI at 7 tesla and above: demonstrated and potential capabilities. J Magn Reson Imaging 41: 13–33. https://doi.org/10.1002/jmri.24573.

Kultas-Ilinsky K, Leontiev V, Whiting PJ (1998). Expression of 10 GABA(A) receptor subunit messenger RNAs in the motor-related thalamic nuclei and basal ganglia of Macaca mulatta studied with in situ hybridization histochemistry. Neuroscience 85: 179–204. Available at http://www.ncbi.nlm.nih.gov/pubmed/9607711.

Kuwajima M et al. (2004). Subcellular and subsynaptic localization of group I metabotropic glutamate receptors in the monkey subthalamic nucleus. J Comp Neurol 474: 589–602. https://doi.org/10.1002/cne.20158.

Ladd ME et al. (2018). Pros and cons of ultra-high-field MRI/MRS for human application. Prog Nucl Magn Reson Spectrosc 109: 1–50, The Authors. https://doi.org/10.1016/j.pnmrs.2018.06.001.

Lambert C et al. (2012). Confirmation of functional zones within the human subthalamic nucleus: patterns of connectivity and sub-parcellation using diffusion weighted imaging. Neuroimage 60: 83–94. https://doi.org/10.1016/j.neuroimage.2011.11.082.

Lambert C et al. (2015). Do we need to revise the tripartite subdivision hypothesis of the human subthalamic nucleus (STN)? Response to Alkemade and Forstmann. Neuroimage, 2015/01/27. 110: 1–2. https://doi.org/10.1016/j.neuroimage.2015.01.038.

Lange H et al. (1976). Morphometric studies of the neuropathological changes in choreatic diseases. J Neurol

Sci 28: 401–425. https://doi.org/10.1016/0022-510X(76)90114-3.

Levesque JC, Parent A (2005). GABAergic interneurons in human subthalamic nucleus. Mov Disord 20: 574–584. https://doi.org/10.1002/mds.20374.

Logan GD, Cowan WB, Davis KA (1984). On the ability to inhibit simple and choice reaction time responses: a model and a method. J Exp Psychol Hum Percept Perform 10: 276–291. https://doi.org/10.1037/0096-1523.10.2.276.

Lozano AM et al. (2019). Deep brain stimulation: current challenges and future directions. Nat Rev Neurol 15: 148–160, Nature Publishing Group. https://doi.org/10.1038/s41582-018-0128-2.

Makris N et al. (2013). Volumetric parcellation methodology of the human hypothalamus in neuroimaging: normative data and sex differences. Neuroimage, 2012/12/19. 69: 1–10. https://doi.org/10.1016/j.neuroimage.2012.12.008.

Massey LA et al. (2012). High resolution MR anatomy of the subthalamic nucleus: imaging at 9.4 T with histological validation. Neuroimage, 2011/11/01. 59: 2035–2044. https://doi.org/10.1016/j.neuroimage.2011.10.016.

Middleton FA, Strick PL (2000). Basal ganglia and cerebellar loops: motor and cognitive circuits. Brain Res Brain Res Rev 31: 236–250. Available at http://www.ncbi.nlm.nih.gov/pubmed/10719151.

Morel A et al. (2002). Neurochemical organization of the human basal ganglia: anatomofunctional territories defined by the distributions of calcium-binding proteins and SMI-32. J Comp Neurol 443: 86–103, John Wiley & Sons, Ltd. https://doi.org/10.1002/cne.10096.

Mori S et al. (1985). Immunohistochemical demonstration of serotonin nerve fibers in the subthalamic nucleus of the rat, cat and monkey. Neurosci Lett 62: 305–309. Available at http://www.ncbi.nlm.nih.gov/pubmed/2419795.

Mulder MJ et al. (2019). Size and shape matter: the impact of voxel geometry on the identification of small nuclei. PLoS One 14: e0215382. https://doi.org/10.1371/journal.pone.0215382. Edited by N. Bergsland. Public Library of Science.

Nauta HJ, Cole M (1978). Efferent projections of the subthalamic nucleus: an autoradiographic study in monkey and cat. J Comp Neurol 180: 1–16. https://doi.org/10.1002/cne.901800102.

Nowinski WL et al. (2005). Statistical analysis of 168 bilateral subthalamic nucleus implantations by means of the probabilistic functional atlas. Neurosurgery 57: 319–330. https://doi.org/10.1227/01.NEU.0000180960.75347.11.

Ogawa S et al. (1990). Brain magnetic resonance imaging with contrast dependent on blood oxygenation. Proc Natl Acad Sci U S A 87: 9868–9872, National Academy of Sciences. https://doi.org/10.1073/pnas.87.24.9868.

Parent A, Hazrati LN (1995). Functional anatomy of the basal ganglia. I. The cortico-basal ganglia-thalamo-cortical loop. Brain Res Brain Res Rev 20: 91–127. Available at http://www.ncbi.nlm.nih.gov/pubmed/7711769.

Parent A et al. (1996). Calcium-binding proteins in primate basal ganglia. Neurosci Res 25: 309–334. Available at http://www.ncbi.nlm.nih.gov/pubmed/8866512.

Parent M et al. (2011). Serotonin innervation of basal ganglia in monkeys and humans. J Chem Neuroanat 41: 256–265. https://doi.org/10.1016/j.jchemneu.2011.04.005.

Pierpaoli C (2010). Quantitative brain MRI. Top Magn Reson Imaging 21: 63, NIH Public Access. https://doi.org/10.1097/RMR.0b013e31821e56f8.

Plantinga BR et al. (2016). Ultra-high field MRI post mortem structural connectivity of the human subthalamic nucleus, substantia nigra, and globus pallidus. Front Neuroanat Frontiers Media SA, 10: 66. https://doi.org/10.3389/fnana.2016.00066.

Rafols JA, Fox CA (1976). The neurons in the primate subthalamic nucleus: a Golgi and electron microscopic study. J Comp Neurol 168: 75–111. https://doi.org/10.1002/cne.901680105.

Raynor K, Kong H, Mestek A et al. (1995). Characterization of the cloned human mu opioid receptor. J Pharmacol Exp Ther 272: 423–428. Available at http://www.ncbi.nlm.nih.gov/pubmed/7815359.

Redgrave P, Prescott TJ, Gurney K (1999). The basal ganglia: a vertebrate solution to the selection problem? Neuroscience 89: 1009–1023. Available at http://www.ncbi.nlm.nih.gov/pubmed/10362291.

Schafer A et al. (2012). Direct visualization of the subthalamic nucleus and its iron distribution using high-resolution susceptibility mapping. Hum Brain Mapp 33: 2831–2842. https://doi.org/10.1002/hbm.21404.

Schmierer K et al. (2008). Quantitative magnetic resonance of postmortem multiple sclerosis brain before and after fixation. Magn Reson Med 59: 268–277, Wiley Subscription Services, Inc., A Wiley Company, 59: 268–277. https://doi.org/10.1002/mrm.21487.

Smith Y, Parent A (1988). Neurons of the subthalamic nucleus in primates display glutamate but not GABA immunoreactivity. Brain Res 453: 353–356. Available at: http://www.ncbi.nlm.nih.gov/pubmed/2900056.

Smith Y, Hazrati LN, Parent A (1990). Efferent projections of the subthalamic nucleus in the squirrel monkey as studied by the PHA-L anterograde tracing method. J Comp Neurol 294: 306–323. https://doi.org/10.1002/cne.902940213.

Stüber C et al. (2014). Myelin and iron concentration in the human brain: a quantitative study of MRI contrast. Neuroimage 93: 95–106. https://doi.org/10.1016/j.neuroimage.2014.02.026.

Sun H et al. (2015). Validation of quantitative susceptibility mapping with Perls' iron staining for subcortical gray matter. NeuroImage 105: 486–492, Academic Press. https://doi.org/10.1016/J.NEUROIMAGE.2014.11.010.

Trattnig S et al. (2018). Key clinical benefits of neuroimaging at 7 T. Neuroimage 168: 477–489. https://doi.org/10.1016/j.neuroimage.2016.11.031.

van Duijn S et al. (2011). MRI artifacts in human brain tissue after prolonged formalin storage. Magn Reson Med 65: 1750–1758. https://doi.org/10.1002/mrm.22758.

von Bonin G, Shariff GA (1951). Exteapyramidal nuclei among mammals. A quantitative study. J Comp Neurol 94: 427–438, John Wiley & Sons, Ltd. https://doi.org/10.1002/cne.900940306.

Weiss M et al. (2015). Spatial normalization of ultrahigh resolution 7 T magnetic resonance imaging data of the postmortem human subthalamic nucleus: a multistage approach. Brain Struct Funct 220: 1695–1703, Springer Berlin Heidelberg. https://doi.org/10.1007/s00429-014-0754-4.

Yelnik J, Percheron G (1979). Subthalamic neurons in primates: a quantitative and comparative analysis. Neuroscience 4: 1717–1743. https://doi.org/10.1016/0306-4522(79)90030-7.

Zwirner J et al. (2017). Subthalamic nucleus volumes are highly consistent but decrease age-dependently-a combined magnetic resonance imaging and stereology approach in humans. Hum Brain Mapp John Wiley & Sons, Ltd 38: 909–922. https://doi.org/10.1002/hbm.23427.